Kirkuk Journal of Science Vol. 21, Iss. 2, p. 24-39, 2026 doi:10.32894/kujss.2026.169539.1293

Structural and Electronic Characterization of Two Indole-Derived Schiff Bases: A Combined Experimental and DFT Study

Zahraa Talib Ghaleb*, Naglaa Jalil Khalil , Nashwan Omar Tapabashi

Department of Chemistry, College of Sciences, University of Kirkuk, Kirkuk, Iraq.
*Corresponding author : zahra@uokirkuk.edu

Article Information

Article Type:
Research Article

Keywords:
($C_{17}H_{15}N_3O$) (Indole-based hydrazone derivative), ($C_{17}H_{14}BrN_3O$) (Bromo-substituted indole hydrazone), structural properties DFT, UV-Vis, FT-IR, TD-DFT.

History:
Received: 18 February 2026
Reviced: 17 April 2026
Accepted: 18 April 2026
Published Online: 30 June 2026

Citation: Zahraa Talib Ghaleb, Naglaa Jalil Khalil, Nashwan Omar Tapabashi, Structural and Electronic Characterization of Two Indole-Derived Schiff Bases: A Combined Experimental and DFT Study, Kirkuk Journal of Science, 21(2), p.24-39, 2026, https://doi.org/10.32894/kujss.2026.169539.1293

Abstract

This study investigates the synthesis and characterization of indole derivatives ($C_{17}H_{15}N_3O$) and ($C_{17}H_{14}BrN_3O$) employing the Density Functional Theory. Experimental characterization using both Infrared and Ultraviolet-Visible techniques was done on synthesized compounds resulting from the formation of hydrazones and yielding information on functional groups, electronic transitions, and structural characteristics. DFT/B3LYP calculations using both (STO-3G*) and (3-21G) basis sets were used for the molecular geometry optimization, Mulliken charge distribution, vibrational spectral simulations, and orbital energies. From the comparison of the two basis sets, it was indicated that the (3-21G) can produce results closer to the experimental results, especially for bond length, vibrational frequency, and electronic transitions. Accordingly, the combined use of both methods provides for the assignment of structural parameters with the utmost precision, charge distribution interpretations with utmost reliability, and a better understanding of molecular stability. This combined approach further emphasizes the role played in computational chemistry to supplement and establish spectroscopic observations of systems made of heterocycles such as indole derivatives. We observe good agreement between the theoretical and experimental results regarding the structural and electronic properties, where (λ_{max})UV-Vis absorption spectrum (Theo) (DFT/B3LYP, STO-3G*-268.95 nm, 3-21G -282.92 nm, expt -282 nm) for the first compound and ((Theo)(DFT/B3LYP, STO-3G*-286.85 nm, 3-21G -289.24 nm, expt -288 nm)) for the second compound.

1. Introduction:

Indole constitutes a bicyclic aromatic heterocycle with a fused benzene-pyrrole system, and its chemical significance in natural and synthetic compounds has been extensively documented [1]. Biochemically, it is the indole of key biomolecules such as tryptophan and indole-3-acetic acid [1]. Due to their important biological and medicinal properties, indole derivatives are of primary interest in drug design and functional materials [2]. Structural alterations on the indole core greatly affect its electronic properties and spectroscopic behavior; hence, they require a comprehensive characterization [2].

The vibrational data acquired from infrared spectroscopy are most useful for indoles, as the N–H bands appear close to 3400 cm^{-1} and the aromatic C=C bands appear around 1500-1600 cm^{-1} [3]. Some vibrational studies have shown that substitution patterns modify IR frequencies in very predictable ways [4]. The behavior of substances in UV-vis spectra is comparable to $\pi \rightarrow \pi^*$ absorption, in this case, between 270-290 nm, with the effect of substituents and solvent factors [4].

A relationship could still be obtained through experimental means [3]. NMR ^{1}H and ^{13}C spectroscopy is very important in supporting structural elucidation in the context that aromatic protons resonate around 6.8–8.0 ppm, while carbons are found up to 100-140 ppm [4]. NMR shifts are very electronically sensitive; thus, it is not possible to reveal the substitution pattern present among indole derivatives [3].

The density functional theory (DFT) offers the central theoretical framework in modeling indole geometry, vibrations, and electronic transitions [5]. One of the most proven techniques for organic compounds is the B3LYP functional, which combines back exchange with LYP correlation [6]. The DFT/B3LYP geometry optimization reliably predicts bond lengths, bond angles, and molecular stability of indole systems [7]. Such optimized structures support the calculation of HOMO-LUMO energies, energy gaps, and global reactivity indices [8].

The DFT-generated vibrational frequencies enable direct comparison with the corresponding experimental IR spectra [8], whereas the assignments of vibrational modes have been confirmed with a combined theoretical-experimental methodology [9]. TD-DFT is also used to simulate UV-vis absorption correctly, predict $\pi \rightarrow \pi^*$ and $n \rightarrow \pi^*$ reactions in paragraph (substituted) indoles/groups, and study and address the cross-coupling effects [8]. IR, UV–Vis, and NMR use with DFT/B3LYP calculations constitute a broad framework for the study of indole derivatives from the structural and electronic points of view [3, 8].

Experimental-theoretical hybridization is crucial for the study of stability, charge distribution, and spectroscopic behavior in indole-based systems [9], thereby reinforcing the importance of these systems as valuable models in organic and computational chemistry [1]. From the theoretical DFT/B3LYP results being meaningfully correlated with the experimental observations, this study aims to synthesize indole derivatives and investigate their structural and electronic properties.

2. Computational Methods:

All quantum-chemical calculations were performed with the Gaussian 16 (revision C.01) program [10]. Geometry optimizations, vibrational frequency analyses, Mulliken charge evaluations, orbital energy calculations, and UV excited-state simulations were carried out using density functional theory with the B3LYP functional [7, 11]. Two basis sets, namely STO-3G* and 3-21G, were used for the comparison of structural and electronic results [12, 13]. Geometric structures were initially built and pre-optimized, followed by full optimization at B3LYP/STO-3G* and B3LYP/3-21G levels.

Frequency calculations confirmed the absence of imaginary modes, thereby yielding harmonic IR data to be compared with experimental data [14]. Mulliken population analysis was used for the determination of atomic charges [15], and energies of HOMO and LUMO were obtained for electronic structure and stability evaluations [16]. UV–Vis absorption properties using TD-DFT were computed on the ten lowest single transitions to correlate with spectra obtained experimentally [17, 18]. Scaled harmonic frequencies and IR intensities were assigned to specific vibrational modes using a method proposed by [14, 3].

Electronic distributions and surfaces of molecular orbitals were visualized using the software Multi wave length and Gauss View [19]. All energies are presented in Hartrees or electronvolts, and optimized geometries in Angstroms and degrees. Thermal corrections were applied, when necessary, by means of standard statistical thermodynamic procedures at 298.15 K [20].

3. Experimental Details:

A solution of indole-3-acetic hydrazide (1.0 g, 0.005 mol) in 10 mL of ethanol was prepared. To this, equal amounts (0.005 mol) of the corresponding substituted aldehydes were added: 4-bromobenzaldehyde (0.92 g), 4-chlorobenzaldehyde (0.61 g), 4-hydroxybenzaldehyde (0.61 g), 4-nitrobenzaldehyde (4-nitrobenzaldehyde) (0.75 g).4-(dimethylamino) benzaldehyde (0.75 g), benzaldehyde (0.53 g), salicylaldehyde (0.61 g), anisaldehyde (0.68 g), and 2,4-dimethoxybenzaldehyde (0.83 g).

Each aldehyde was dissolved separately in 10 mL of ethanol containing two drops of glacial acetic acid (GAA) and slowly added to the hydrazide solution with constant stirring until a clear homogeneous mixture was obtained. The reaction mixture was then stirred and heated at 80 °C for 6 h. After completion, the resulting precipitate was collected by filtration, washed thoroughly with cold distilled water, dried and rehydrated with 75% ethanol to obtain the corresponding hydrazone derivatives.

4. Results and Discussion:

4.1 Molecular Geometry:

The complete molecular geometry optimization process resulted in the creation of advanced molecular structures, which are displayed in Figure 1. The molecular structures of CHNO and CHBrNO were examined through density functional theory analysis at the B3LYP level using two different basis sets (STO-3G) and (3-21G) according to the information presented in Figure 1 and Table 1, which includes Parts I and II.

The study uses bond length measurements along with bond angle measurements and dihedral angle measurements to evaluate how different basis set qualities affect the accuracy of optimized geometric measurements. Because the (STO-3G) basis set computes bond distances for C–H and heteroatomic bonds (C–N and C=O) using its most fundamental bonding character, it generates bond lengths that surpass actual measurements. The (3-21G) basis set delivers bond

distance measurements that are shorter than actual values but provide better accuracy because it shows electron density distribution more precisely. The (3-21G) calculates bond angles that differ slightly from actual values but maintain consistent differences through all measurements because the method handles electron delocalization better while creating less angular strain.

The dihedral angle analysis results show that (3-21G) provides better performance for describing torsional movements in flexible areas of the material than (STO-3G), which fails to accurately represent torsional low points. The introduction of a bromine substituent results in observable geometric transformations that stem from both steric effects and electronic effects, yet the aromatic structure maintains its basic planar form to protect π-conjugation. The (3-21G) prediction of a longer C–Br bond length matches with bromine's large atomic radius and high polarizability properties. The (STO-3G) and (3-21G) models show different results because they handle electronic polarization and torsional effects in different ways, with the split-valence basis set delivering a more accurate representation of molecular geometry, which correlates well with earlier experimental and theoretical studies [21, 22].

4.2 Mullikan Charge:

4.2.1 $C_{17}H_{15}N_3O$:

Figure 2 presents the Mulliken charge distribution results for compound A1 which were obtained through DFT/B3LYP calculations using both (STO-3G*) and (3-21G) basis sets to study how different basis set options affect electron density distribution. The results show that (STO-3G*) produces lower absolute charge values while (3-21G) shows increased charge separation because it better represents polarization and lone-pair characteristics.

The carbon atoms show only slight changes from their original state but the carbon atoms near conjugated and heteroatomic centers display increased positive charge which shows better π-electron delocalization representation through (3-21G). The (3-21G) results show higher positive charges for hydrogen atoms because they exhibit stronger bond polarization between C–H and X–H bonds where X represents either nitrogen or oxygen. The most pronounced differences occur at heteroatoms: nitrogen and oxygen atoms display significantly more negative charges with (3-21G), which improves the description of lone-pair localization together with electronegativity effects. The changes provide a more accurate representation of electronic structure which scientists need to study reactivity and hydrogen-bonding ability and intermolecular interaction. The minimal (STO-3G) base set underestimates charge values because its capacity to simulate polarization effects stands at an insufficient level. The (3-21G) basis set delivers a more accurate representation of Mulliken charge distribution for π-conjugated systems with heteroatoms, which matches the findings of earlier theoretical research [23, 24, 25, 26, 27].

4.2.2 $C_{17}H_{14}BrN_3O$:

Figure 3 displays the Mulliken charge distribution for compound A2, which was computed at the DFT/B3LYP level using both the (STO-3G*) and (3-21G) basis sets, to demonstrate how different basis-set quality affects electronic structure descriptions. The (3-21G) basis set produces greater absolute charge values and better polarization results than (STO-3G*) because it provides superior ability to represent valence electron density. The (3-21G) results show that nitrogen and oxygen atoms have greater negative charges which better represent their ability to localize lone pairs and their electron-withdrawing properties that scientists need to evaluate molecular reactivity and hydrogen-bonding strength.

The two basis sets produce only minor differences for aromatic carbon atoms but specific locations show greater charge separation through (3-21G) which results from better treatment of conjugation and inductive effects. The hydrogen atoms that bond with aromatic and heteroatomic centers demonstrate increased positive charge through (3-21G) because stronger bond polarization exists in this bond. The split-valence basis set delivers a more accurate description of bromine's atomic structure because it can effectively represent the atom's extensive electron cloud which includes polarizable material. The (STO-3G*) method underestimates charge values because of its simple design whereas (3-21G) delivers a better chemical explanation of charge distribution in A2 which matches earlier theoretical research findings [23, 24, 25, 26, 27].

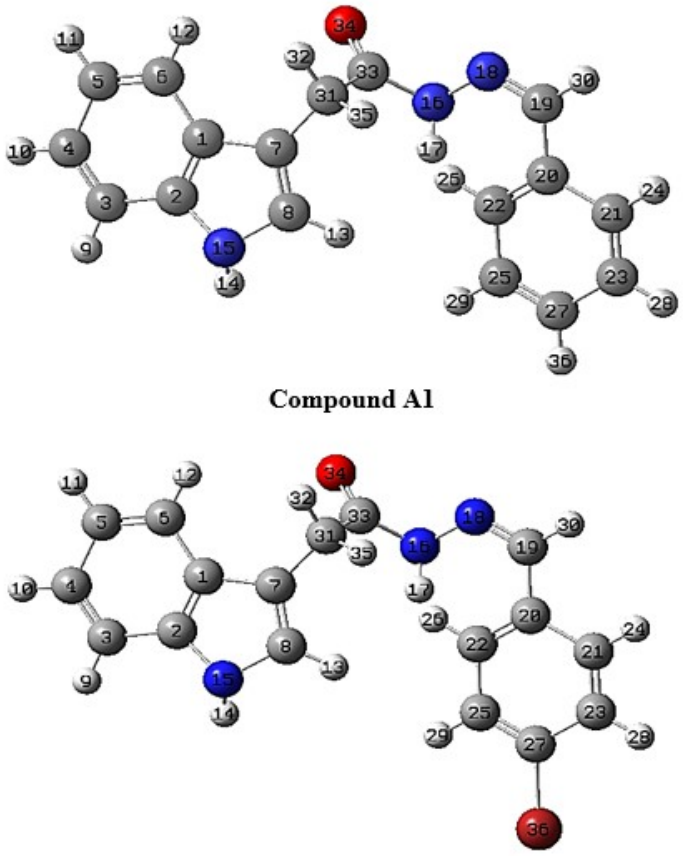

Figure 1. Optimized molecular geometries and atomic numbering of Compounds A1($C_{17}H_{15}N_3O$) and A2 ($C_{17}H_{14}BrN_3O$) (White hydrogen, gray carbon, red oxygen, blue nitrogen, dark red bromine).

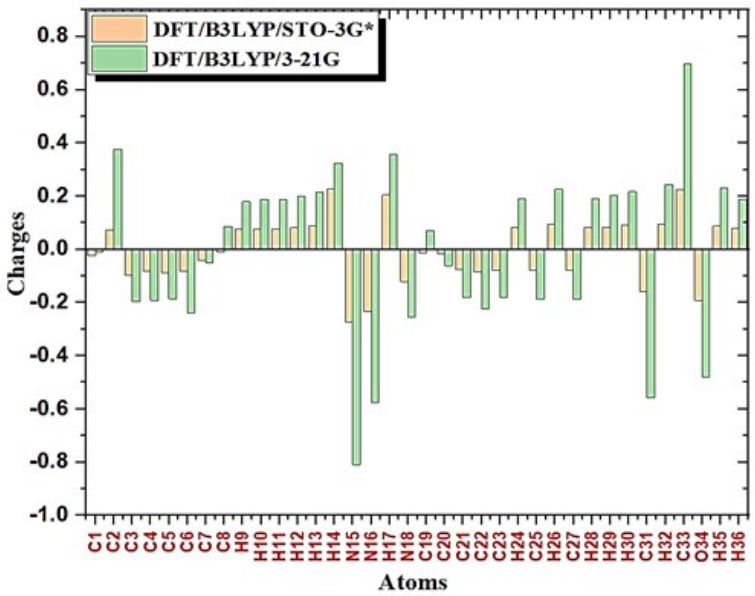

Figure 2. The Mulliken charge distribution for the A1($C_{17}H_{15}N_3O$) molecule using DFT/B3LYP (STO-3G* and 3-21G).

Table 1. Optimized geometric parameter of compound (A1 and A2) using (DFT/B3LYP / STO-3G* and DFT/B3LYP /3-21G).

A1 $C_{17}H_{15}N_3O$ DFT/B3LYP (gas-phase)								
Bond length (Å)	STO-3G*	3-21G	Angle length (°)	STO-3G*	3-21G	Dihedral angle (°)	STO-3G*	3-21G
R(1,2)	1.437	1.4279	A(2,1,6)	118.6434	119.4161	D(6,1,2,3)	-0.0445	-0.4259
R(1,6)	1.4223	1.4048	A(2,1,7)	107.5956	107.2304	D(6,1,2,15)	179.8221	179.1605
R(1,7)	1.4642	1.451	A(6,1,7)	133.7609	133.342	D(7,1,2,3)	179.8248	-179.3506
R(2,3)	1.4176	1.3989	A(1,2,3)	122.5047	121.5568	D(7,1,2,15)	-0.3085	0.2358
R(2,15)	1.415	1.3857	A(1,2,15)	106.8393	107.1972	D(2,1,6,5)	0.0829	0.2386
R(3,4)	1.3995	1.3914	A(3,2,15)	130.6558	131.2443	D(2,1,6,12)	-179.8276	-179.6854
R(3,9)	1.0974	1.0839	A(2,3,4)	117.2079	117.868	D(7,1,6,5)	-179.7447	178.8264
R(4,5)	1.4254	1.4111	A(2,3,9)	121.2415	121.2772	D(7,1,6,12)	0.3448	-1.0977
R(4,10)	1.0981	1.0837	A(4,3,9)	121.5504	120.8541	D(2,1,7,8)	0.0905	-0.1493
R(5,6)	1.3995	1.3905	A(3,4,5)	121.3349	121.2396	D(2,1,7,31)	-179.0839	-178.7536
R(5,11)	1.0978	1.0834	A(3,4,10)	119.4476	119.4104	D(6,1,7,8)	179.9318	-178.8614
R(6,12)	1.0984	1.084	A(5,4,10)	119.2175	119.3498	D(6,1,7,31)	0.7574	2.5343
R(7,8)	1.3845	1.3767	A(4,5,6)	121.3354	121.0624	D(1,2,3,4)	-0.0362	0.3165
R(7,31)	1.5258	1.5007	A(4,5,11)	118.9748	119.2013	D(1,2,3,9)	-179.8803	-179.3859
R(8,13)	1.096	1.0778	A(6,5,11)	119.6898	119.7363	D(15,2,3,4)	-179.868	-179.158
R(8,15)	1.4161	1.3956	A(1,6,5)	118.9737	118.8559	D(15,2,3,9)	0.2879	1.1396
R(14,15)	1.0414	1.011	A(1,6,12)	120.4145	120.4239	D(1,2,15,8)	0.4127	-0.2354
R(16,17)	1.0556	1.0205	A(5,6,12)	120.6118	120.7202	D(1,2,15,14)	178.6066	-179.5521
R(16,18)	1.4466	1.4014	A(1,7,8)	106.9764	106.5691	D(3,2,15,8)	-179.7355	179.2959
R(16,33)	1.4627	1.3841	A(1,7,31)	126.6875	126.6788	D(3,2,15,14)	-1.5416	-0.0209
R(18,19)	1.3369	1.2946	A(8,7,31)	126.3305	126.7358	D(2,3,4,5)	0.0788	-0.0317
R(19,20)	1.5045	1.4786	A(7,8,13)	130.2578	129.1563	D(2,3,4,10)	-179.9203	-179.8614
R(19,30)	1.1034	1.0875	A(7,8,15)	109.6941	109.8077	D(9,3,4,5)	179.9224	179.672

Continued on next page

A1 $C_{17}H_{15}N_3O$ DFT/B3LYP (gas-phase)								
Bond length (Å)	STO-3G*	3-21G	Angle length (°)	STO-3G*	3-21G	Dihedral angle (°)	STO-3G*	3-21G
R(20,21)	1.4227	1.407	A(13,8,15)	120.0452	121.0332	D(9,3,4,10)	-0.0767	-0.1576
R(20,22)	1.4217	1.4078	A(2,15,8)	108.8929	109.1951	D(3,4,5,6)	-0.0412	-0.1473
R(21,23)	1.4051	1.3928	A(2,15,14)	125.7359	125.6414	D(3,4,5,11)	179.9355	179.9224
R(21,24)	1.0987	1.0849	A(8,15,14)	125.3443	125.1597	D(10,4,5,6)	179.9579	179.6825
R(22,25)	1.4078	1.3957	A(17,16,18)	118.531	121.3655	D(10,4,5,11)	-0.0654	-0.2478
R(22,26)	1.098	1.0828	A(17,16,33)	115.7372	119.3794	D(4,5,6,1)	-0.0427	0.0386
R(23,27)	1.4106	1.3985	A(18,16,33)	116.4198	119.0438	D(4,5,6,12)	179.8676	179.9624
R(23,28)	1.0985	1.084	A(16,18,19)	114.5492	118.4633	D(11,5,6,1)	179.9808	179.9686
R(25,27)	1.4087	1.3962	A(18,19,20)	131.6743	131.1776	D(11,5,6,12)	-0.1089	-0.1076
R(25,29)	1.0985	1.0835	A(18,19,30)	112.6774	113.6528	D(1,7,8,13)	-179.1981	-179.371
R(27,36)	1.0983	1.0839	A(20,19,30)	115.6156	115.1693	D(1,7,8,15)	0.166	0.0065
R(31,32)	1.1053	1.0952	A(19,20,21)	118.3682	118.3182	D(31,7,8,13)	-0.0199	-0.7678
R(31,33)	1.5907	1.5478	A(19,20,22)	123.2093	122.9676	D(31,7,8,15)	179.3443	178.6097
R(31,35)	1.1059	1.0984	A(21,20,22)	118.3621	118.6368	D(1,7,31,32)	47.6402	56.5628
R(33,34)	1.2487	1.2298	A(20,21,23)	120.8941	120.7801	D(1,7,31,33)	-73.4784	-64.3071
			A(20,21,24)	119.1607	119.158	D(1,7,31,35)	165.5019	174.9175
			A(23,21,24)	119.9446	120.0606	D(8,7,31,32)	-131.3797	-121.7678
			A(20,22,25)	120.5271	120.4006	D(8,7,31,33)	107.5017	117.3623
			A(20,22,26)	119.9023	120.4569	D(8,7,31,35)	-13.518	-3.4131
			A(25,22,26)	119.5253	119.0992	D(7,8,15,2)	-0.3674	0.1448
			A(21,23,27)	120.0985	120.0843	D(7,8,15,14)	-178.57	179.4656
			A(21,23,28)	119.8627	119.8694	D(13,8,15,2)	179.072	179.5815
			A(27,23,28)	120.0382	120.0455	D(13,8,15,14)	0.8694	-1.0977
			A(22,25,27)	120.4126	120.3649	D(17,16,18,19)	23.5297	10.2848

Continued on next page

A1 $C_{17}H_{15}N_3O$ DFT/B3LYP (gas-phase)								
Bond length (Å)	STO-3G*	3-21G	Angle length (°)	STO-3G*	3-21G	Dihedral angle (°)	STO-3G*	3-21G
			A(22,25,29)	119.4863	119.0169	D(33,16,18,19)	168.8172	-175.0302
			A(27,25,29)	120.0996	120.6166	D(17,16,33,31)	-14.1688	1.8638
			A(23,27,25)	119.6866	119.7131	D(17,16,33,34)	167.6609	-179.2525
			A(23,27,36)	120.1174	120.0708	D(18,16,33,31)	-160.4305	-172.9285
			A(25,27,36)	120.1916	120.2121	D(18,16,33,34)	21.3992	5.9553
			A(7,31,32)	110.5509	111.4884	D(16,18,19,20)	1.08	4.1598
			A(7,31,33)	115.6964	115.8642	D(16,18,19,30)	-176.7068	-175.6536
			A(7,31,35)	109.5444	109.6757	D(18,19,20,21)	-145.9909	-147.0111
			A(32,31,33)	106.4903	105.6525	D(18,19,20,22)	36.8845	36.2352
			A(32,31,35)	107.1544	107.0244	D(30,19,20,21)	31.7444	32.8001
			A(33,31,35)	107.0111	106.6579	D(30,19,20,22)	-145.3802	-143.9537
			A(16,33,31)	112.1657	112.5737	D(19,20,21,23)	-178.8015	-178.5224
			A(16,33,34)	123.3179	125.0644	D(19,20,21,24)	1.4699	1.887
			A(31,33,34)	124.4889	122.3521	D(22,20,21,23)	-1.5353	-1.6253
						D(22,20,21,24)	178.736	178.784
						D(19,20,22,25)	178.1836	178.0599
						D(19,20,22,26)	0.6443	0.4738
						D(21,20,22,25)	1.0588	1.316
						D(21,20,22,26)	-176.4805	-176.2702
						D(20,21,23,27)	0.7922	0.7595
						D(20,21,23,28)	-179.5156	-179.5605
						D(24,21,23,27)	-179.4813	-179.6535
						D(24,21,23,28)	0.211	0.0264
						D(20,22,25,27)	0.1569	-0.1463

Continued on next page

A1 $C_{17}H_{15}N_3O$ DFT/B3LYP (gas-phase)								
Bond length (Å)	STO-3G*	3-21G	Angle length (°)	STO-3G*	3-21G	Dihedral angle (°)	STO-3G*	3-21G
						D(20,22,25,29)	-179.3935	-179.6847
						D(26,22,25,27)	177.7055	177.4724
						D(26,22,25,29)	-1.8449	-2.066
						D(21,23,27,25)	0.4544	0.4403
						D(21,23,27,36)	179.6987	179.7066
						D(28,23,27,25)	-179.2373	-179.2391
						D(28,23,27,36)	0.007	0.0272
						D(22,25,27,23)	-0.9269	-0.7449
						D(22,25,27,36)	179.8294	179.9899
						D(29,25,27,23)	178.6208	178.7861
						D(29,25,27,36)	-0.6229	-0.4792
						D(7,31,33,16)	-20.695	-23.0725
						D(7,31,33,34)	157.4499	158.009
						D(32,31,33,16)	-143.9745	-147.0321
						D(32,31,33,34)	34.1705	34.0494
						D(35,31,33,16)	101.6797	99.314
						D(35,31,33,34)	-80.1753	-79.6045
(A2) $C_{17}H_{14}BrN_3O$								
R(27,36)	1.888	1.9304	A(23,27,36)	120.0549	119.6915	D(21,23,27,36)	-179.7125	-179.704
			A(25,27,36)	120.0897	119.8337	D(28,23,27,36)	0.425	0.4044
						D(22,25,27,36)	179.2716	179.3967
						D(29,25,27,36)	- 0.9476	-0.8806

End of Table

4.3 Vibrational Frequencies (cm^{-1}):

4.3.1 $C_{17}H_{15}N_3O$:

The researchers used experimental FTIR spectra of $C_{17}H_{15}N_4O$ shown in Figures (4, 5, 6) to evaluate theoretical frequency results, which DFT/B3LYP combined with the (STO-3G*) and (3-21G) basis sets to produce. The absorption bands which appear at 3324 cm^{-1}, 3246 cm^{-1}, and 3213 cm^{-1} in the high-frequency range correspond to N–H stretching vibrations, which confirm that amino or hydrazone-type functional groups are present. The (3-21G) basis set provides superior results because it accurately predicts N-H stretch frequencies, which lie in the 3300-3400 cm^{-1} range, while (STO-3G*) demonstrates a slight frequency underestimation. The 2988 cm^{-1} band displays aromatic/aliphatic C-H stretching, which both basis sets can adequately describe, but 3-21G provides better results for this measurement. The 1723 cm^{-1} absorption peak results from C=O stretching, which (3-21G) can accurately reproduce, whereas (STO-3G*) produces lower frequencies and less intense results. The bands found at 1672, 1610, and 1555 cm^{-1} correspond to C=N stretching, N–H bending, and aromatic C=C vibrations, which demonstrate the presence of a conjugated aromatic–nitrogen system. The 1460–1196 cm^{-1} range contains C–N stretching and in-plane C–H bending modes, while peaks that occur below 1000 cm^{-1} result from ring deformation and out-of-plane C–H bending vibrations. The (3-21G) basis set enables better matching with experimental spectrum data throughout all spectral regions because it outperforms other methods in modeling hydrogen bonding and heteroatom and conjugated system vibrational modes.

4.3.2 $C_{17}H_{14}BrN_3O$:

The experiment used FTIR spectra of $C_{17}H_{14}BrN_3O$, which were recorded in Figures (7, 8, 9) to perform DFT/B3LYP calculations with (STO-3G*) and (3-21G) basis sets to study its vibrational properties and verify its structural characteristics. The 3431 cm^{-1} band shows a strong N–H stretching vibration, indicating the presence of amine or hydrazide functional groups; the theoretical models successfully reproduced this mode with (3-21G), which showed better results than the other model. The absorption at 3053 cm^{-1} corresponds to aromatic C–H stretching and is more accurately described by the split-valence basis set. The carbonyl group C=O stretching creates a strong band at 1658 cm^{-1}, which both basis sets can predict accurately with (3-21G), providing results that match experimental data more closely. The 1600–1450 cm^{-1} range produces bands which come from aromatic C=C stretching and N–H bending vibrations that represent a conjugated aromatic–nitrogen system, and 3-21G produces better results with this particular system. The fingerprint region (1200–1000 cm^{-1}) is associated with C–N stretching modes, while absorptions below 900 cm^{-1} correspond to out-of-plane C–H bending of the substituted aromatic ring. The (3-21G) basis set demonstrates a better match with experimental results according to all modes which involve heteroatoms and aromatic substitution, while (STO-3G*) overestimates low-frequency vibrations according to references [[28, 29]].

4.4 UV-Vis spectrum:

4.4.1 $C_{17}H_{15}N_3O$:

The experimental UV–Vis spectrum of $C_{17}H_{15}N_3O$ Figure 10 shows strong absorption in the 190–350 nm region, which demonstrates electronic transitions for conjugated π systems that have heteroatoms. The spectrum displays two primary absorption bands: a strong band at 200–220 nm and a broader band at 270–280 nm, corresponding to $\pi ß \pi^*$ and n$\rightarrow\pi^*$ transitions from aromatic rings and nitrogen- or oxygen-centered lone pairs. TD-DFT calculations conducted at the B3LYP level using the (STO-3G*) and (3-21G) basis sets provide strong evidence for the existence of these experimental characteristics. The (STO-3G*) basis set predicts a dominant electronic transition near 270 nm, which matches the experimental band and results from a HOMO$\rightarrow$LUMO $\pi ß \pi^*$ excitation. The (3-21G) basis set produces a red-shifted transition at 282 nm because it better describes how excited-state electrons redistribute and how conjugation effects operate. The value shows a slight overestimation but still maintains acceptable experimental accuracy because gas-phase calculations failed to account for solvent and environmental impacts. The (3-21G) basis set provides better accuracy for molecular electronic excitation energy and charge-transfer character than other basis sets.

4.4.2 $C_{17}H_{14}BrN_3O$:

Figure **??** shows the comparison between the experimental results and the theoretical predictions for the UV–Vis spectra of $C_{17}H_{14}BrN_3$. The experimental results show a moderate-to-intense absorption band that starts just below 300 nm. This band primarily results from the $\pi ß \pi^*$ transition in the conjugated aromatic and triazole system. The band shows a minor $n ß \pi^*$ contribution from the lone pairs of heteroatoms. The TD-DFT calculations showed that the B3LYP level predicted the main electronic transition to occur at 287 nm with the (STO-3G*) basis set and at 289 nm with the (3-21G) basis set. The experimental maximum was closely matched by both predicted transitions. The (3-21G) basis set produced a small red shift because it better captured the valence orbital flexibility and excited-state electron delocalization. The calculated and experimental spectra show their main differences because vibronic coupling, solvent effects, and band broadening exceed the limits of gas-phase vertical excitation calculations. The two basis sets capture the main experimental feature, but the (3-21G) basis set shows better accuracy for wavelength and intensity measurements, which makes it the better choice for quantitative UV–Vis predictions in brominated, heteroatom-containing conjugated systems [[30, 31, 32]].

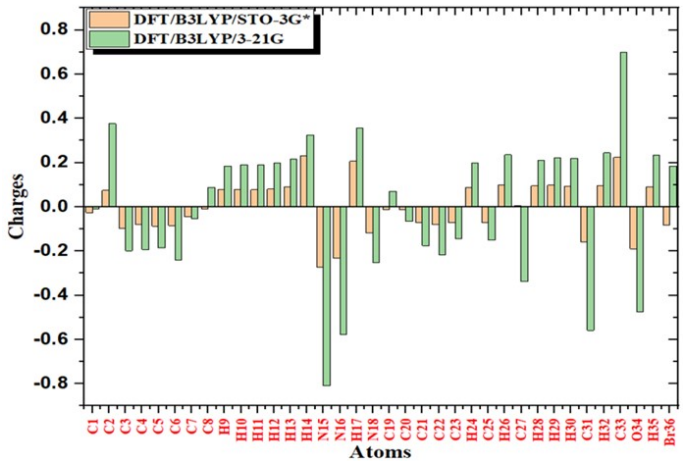

Figure 3. The Mulliken charge distribution for the (A2) ($C_{17}H_{14}BrN_3O$) molecule using DFT/B3LYP (STO-3G* and 3-21G).

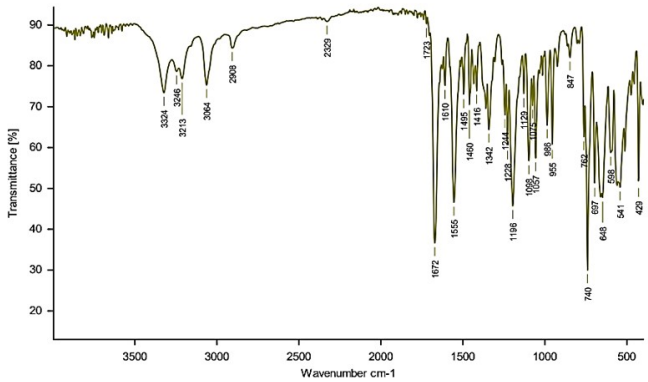

Figure 4. Experimental IR spectrum of compound A1 ($C_{17}H_{15}N_4O$).

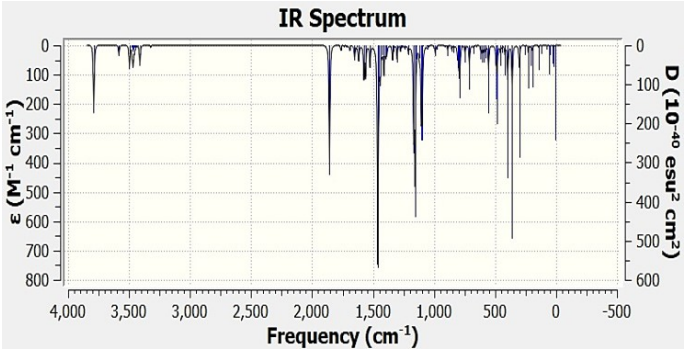

Figure 5. Theoretical IR spectrum of compound A1 ($C_{17}H_{15}N_4O$) using (DFT/B3LYP/STO-(DFT/B3LYP/STO-3G*).

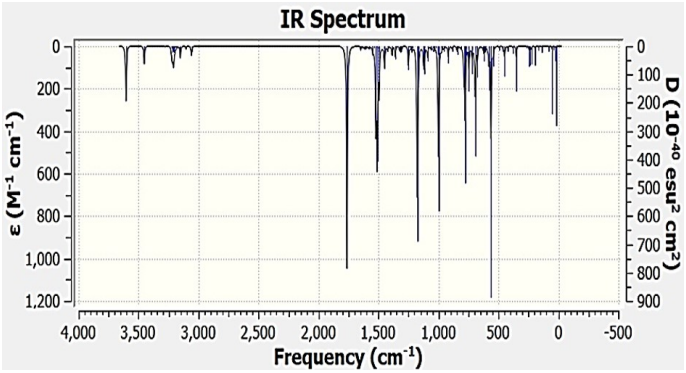

Figure 6. Theoretical IR spectrum of compound A1 ($C_{17}H_{15}N_4O$) using(DFT/B3LYP/STO-(DFT/B3LYP/3-21G).

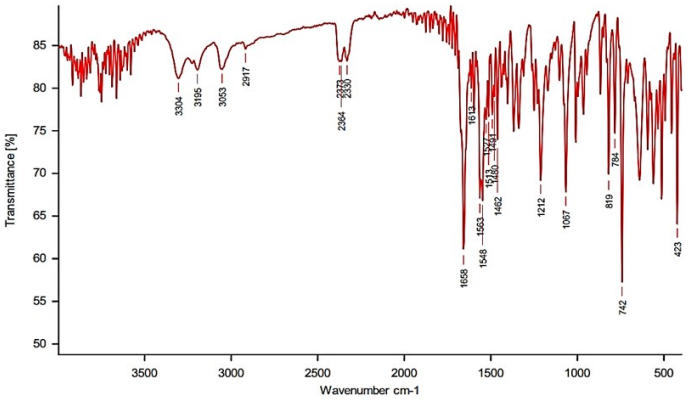

Figure 7. Experimental IR spectrum of compound A2 ($C_{17}H_{14}BrN_3O$).

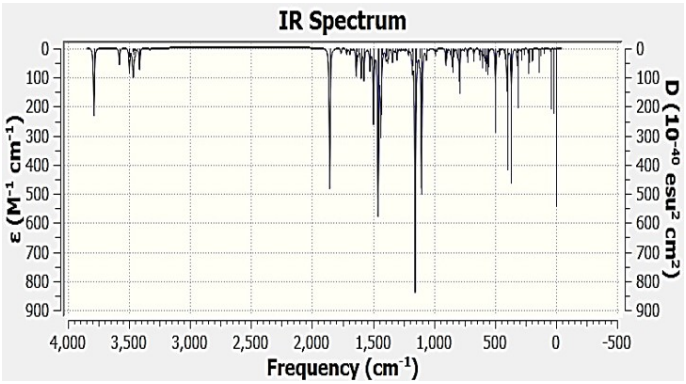

Figure 8. Theoretical IR spectrum of compound A2 ($C_{17}H_{14}BrN_3O$) using (DFT/B3LYP/STO-3G*).

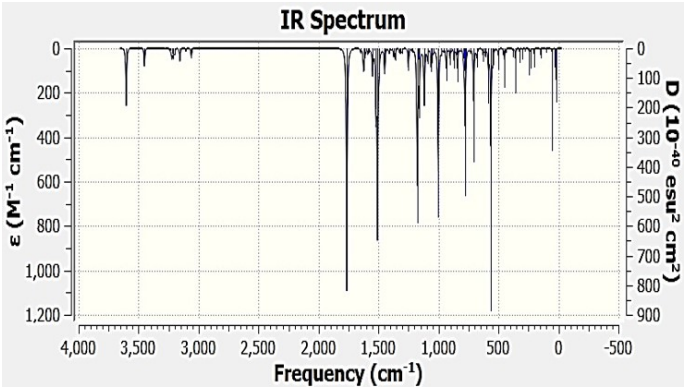

Figure 9. Theoretical IR spectrum of compound A2 ($C_{17}H_{14}BrN_3O$) using (DFT/B3LYP/3-21G).

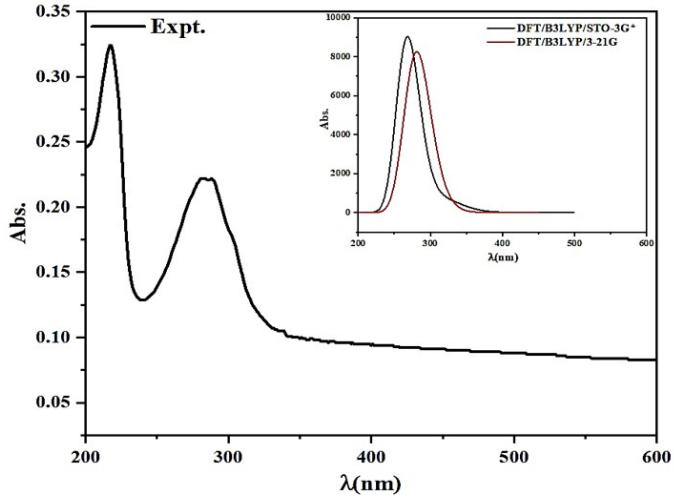

Figure 10. Experimental UV-Vis absorption spectrum compared with theoretical results calculated at DFT/B3LYP/STO-3G* and DFT/B3LYP/3-21G levels for $C_{17}H_{15}N_3O$.

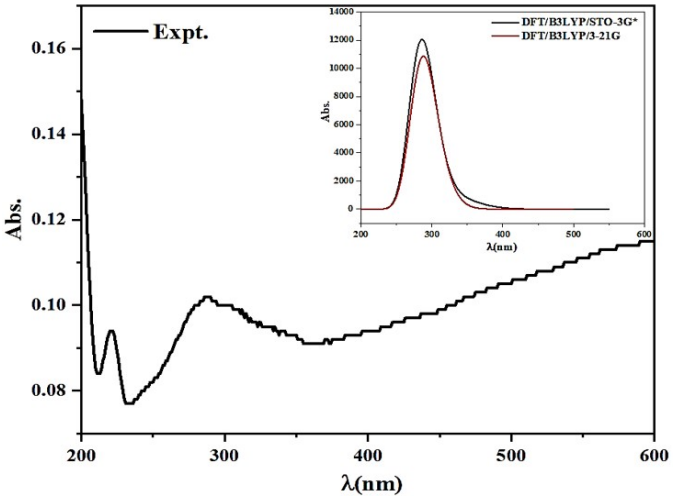

Figure 11. Experimental UV-Vis absorption spectrum compared with theoretical results calculated at DFT/B3LYP/STO-3G* and DFT/B3LYP/3-21G levels for ($C_{17}H_{14}BrN_3O$).

5. Conclusion:

This dual experimental and computational work characterizes the coherent structural and electronic behavior of the synthesized indole derivatives (A1 and A2). From experimental IR, there is confirmation of other specific functional groups, while UV-Vis measurements act as ancillary evidential sources in determining substitution patterns for the studied molecules. The DFT/B3LYP calculations also provide an additional contribution in establishing optimized geometries, Mulliken charge distributions, vibrational frequencies, and energies of the frontier orbitals, providing more ground for interpretation of the stability and reactivity of the various compounds. Of the two basis sets, (3-21-G) was the most consistent in providing stronger correlation with direct experimental data and hence, claimed increased accuracy as compared to (STO-3G*). Besides this, an analysis of HOMO-LUMO gaps and electron density distribution has enlightened the electronic behavior of the compounds and their propensity for undergoing chemical interactions. Indeed, the experimental and theoretical data are interspersed to convince themselves of the structures of the molecules, explain the physicochemical properties of indoles, and reiterate the powerful impact of coupling spectroscopic with computational practices on modern chemical research. The optimized geometries, Mulliken charge distributions, vibration frequency, and electronic properties simulated using computational methods are in agreement with available experimental data for compound A; they can be used to predict properties of similar compounds with a reasonably high degree of accuracy.

Funding: None .

Data Availability Statement: All data supporting the findings of this study are available from the corresponding author upon request.

Declarations:

Conflict of interest: The authors declare no conflicts of interest.

Ethical approval: This study did not involve human or animal subjects; therefore, ethical approval was not required.

Author contributions: Zahraa T. Ghaleb: conceptualization, methodology, software , validation, formal analysis, investigation, resources, data curation, and writing original draft. Naglaa Jalil Khalil and Nashwan Omar Tapabashi: review, editing, and supervision.

References

[1] Ashok Kumar Yadav, Shobhit Srivastava, Bhumika Yogi, and Sujeet Kumar Gupta. Isatin: A versatile heterocyclic compound a review. *Chemistry Research Journal*, 7(2):33–42, 2022.

[2] Xingyou Mo, Devendra Pratap Rao, Kirandeep Kaur, Roket Hassan, Ahmed S Abdel-Samea, Sara Mahmoud Farhan, Stefan Bräse, and Hamada Hashem. Indole derivatives: a versatile scaffold in modern drug discovery—an updated review on their multifaceted therapeutic applications (2020–2024). *Molecules*, 29(19):4770, 2024, doi:10.3390/molecules29194770.

[3] Uzma Younis, Ashfaq Ahmad Rahi, Subhan Danish, Muhammad Arif Ali, Niaz Ahmed, Rahul Datta, Shah Fahad, Jiri Holatko, Tereza Hammerschmiedt, Martin Brtnicky, et al. Fourier transform infrared spectroscopy vibrational bands study of spinacia oleracea and trigonella corniculata under biochar amendment in naturally contaminated soil. *PLoS One*, 16(6):e0253390, 2021, doi:10.1371/journal.pone.0253390.

[4] Lampman G. M. Kriz G. S. Vyvyan J. R. Pavia, D. L. *Introduction to spectroscopy*. Cengage Learning, 2015.

[5] Axel D Becke. Density-functional thermochemistry. iii. the role of exact exchange. *The Journal of chemical physics*, 98(7):5648–5652, 1993, doi:10.1063/1.464913.

[6] Chengteh Lee, Weitao Yang, and Robert G Parr. Development of the colle-salvetti correlation-energy formula into a functional of the electron density. *Physical review B*, 37(2):785, 1988, doi:10.1103/PhysRevB.37.785.

[7] Krishnan Raghavachari. Perspective on "density functional thermochemistry. iii. the role of exact exchange" becke ad (1993) j chem phys 98: 5648–52. *Theoretical Chemistry Accounts*, 103(3):361–363, 2000, doi:10.1007/s002140050551.

[8] Sulochana Devar, Vijayalaxmi Gangadharmath, NG Yernale, BS Mathada, Omnath Patil, PK Ingalagondi, and SM Hanagodimath. Studies on molecular structure, uv visible, nmr and homo-lumo of indole derivative using dft calculation. In *AIP Conference Proceedings*, volume 2901, page 040038. AIP Publishing LLC, 2023, doi:10.1063/5.0181309.

[9] María A Muñoz, Pilar Guardado, José Hidalgo, Carmen Carmona, and Manuel Balón. An experimental and theoretical study of the acid-base properties of substituted indoles. *Tetrahedron*, 48(28):5901–5914, 1992, doi:10.1016/S0040-4020(01)90244-6.

[10] MJ ea Frisch, GW Trucks, H Bernhard Schlegel, GE Scuseria, MAn Robb, JR Cheeseman, G Scalmani, VPGA Barone, GA Petersson, HJRA Nakatsuji, et al. Gaussian 16, 2016.

[11] Chengteh Lee, Weitao Yang, and Robert G Parr. Development of the colle-salvetti correlation-energy formula into a functional of the electron density. *Physical review B*, 37(2):785, 1988, doi:10.1103/PhysRevB.37.785.

[12] Warren J Hehre, Robert Ditchfield, and John A Pople. Self—consistent molecular orbital methods. xii. further extensions of gaussian—type basis sets for use in molecular orbital studies of organic molecules. *The Journal of Chemical Physics*, 56(5):2257–2261, 1972, doi:10.1063/1.1677527.

[13] J Stephen Binkley, John A Pople, and Warren J Hehre. Self-consistent molecular orbital methods. 21. small split-valence basis sets for first-row elements. *Journal of the American Chemical Society*, 102(3):939–947, 1980, doi:10.1021/ja00523a008.

[14] Anthony P Scott and Leo Radom. Harmonic vibrational frequencies: an evaluation of hartree- fock, møller-plesset, quadratic configuration interaction, density functional theory, and semiempirical scale factors. *The Journal of Physical Chemistry*, 100(41):16502–16513, 1996, 10.1021/jp960976r.

[15] Robert S Mulliken. Electronic population analysis on lcao–mo molecular wave functions. i. *The Journal of chemical physics*, 23(10):1833–1840, 1955, doi:10.1063/1.1740588.

[16] Robert G Parr. Density functional theory of atoms and molecules. In *Horizons of Quantum Chemistry: Proceedings of the Third International Congress of Quantum Chemistry Held at Kyoto, Japan, October 29-November 3, 1979*, pages 5–15. Springer, 1989,doi:10.1007/978-94-009-9027-2$_2$.

[17] Erich Runge and Eberhard KU Gross. Density-functional theory for time-dependent systems. *Physical review letters*, 52(12):997, 1984, doi:10.1103/PhysRevLett.52.997.

[18] Mark E Casida. Time-dependent density functional response theory for molecules. In *Recent Advances In Density Functional Methods: (Part I)*, pages 155–192. World Scientific, 1995.

[19] Tian Lu and Feiwu Chen. Multiwfn: A multifunctional wavefunction analyzer. *Journal of computational chemistry*, 33(5):580–592, 2012, doi:10.1002/jcc.22885.

[20] Christopher J Cramer. *Essentials of computational chemistry: theories and models*. John Wiley & Sons, 2013.

[21] CS Dileep, MMM Abdoh, MP Chakravarthy, KN Mohana, and MA Sridhar. 1h-indole-3-carbaldehyde. *Structure Reports*, 68(11):o3135–o3135, 2012, doi:10.1107/S1600536812045306.

[22] Ibrahim Omotayo Asiata, Dyebamiyi Abel Kolawole, and Semire Banjo. Molecular charge distributions, vibrational frequency and stability studies on lh-indoie-3-carbaldehyde and (z)-indol-3-ylidenemethanol: Dft approach. *Iraqi National Journal Of Chemistry*, 18(1), 2018.

[23] John Norman Murrell, Sidney Francis Alan Kettle, and John Michael Tedder. The chemical bond. *(No Title)*, 1985.

[24] Banjo Semire, Oluwatumininu Abosede Mutiu, and Abel Kolawole Oyebamiji. Dft and ab initio methods on nmr, ir and reactivity indices of indol-3-carboxylate and indazole-3-carboxylate derivatives of cannabinoids: comparative study. *Journal of Physical Theoretical Chemistry, IAU Iran*, 2017.

[25] C Grüber and V Buss. Quantum-mechanically calculated properties for the development of quantitative structure-activity relationships (qsar's). pka-values of phenols and aromatic and aliphatic carboxylic acids. *Chemosphere*, 19(10-11):1595–1609, 1989, doi:10.1016/0045-6535(89)90173-0.

[26] Ramon Carbó-Dorca and Patrick Bultinck. Quantum mechanical basis for mulliken population analysis. *Journal of mathematical chemistry*, 36(3):231–239, 2004, doi:10.1023/B:JOMC.0000033215.50137.ef.

[27] Jordan J Philips, Mathew A Hudspeth, Philip M Browne Jr, and Juan E Peralta. Basis set dependence of atomic spin populations. *Chemical Physics Letters*, 495(1-3):146–150, 2010, doi:10.1016/j.cplett.2010.07.037.

[28] Ferenc Billes, Paula Veronica Podea, Ildikó Mohammed-Ziegler, Monica Toşa, Hans Mikosch, and Dan-Florin Irimie. Formyl-and acetylindols: Vibrational spectroscopy of an expectably pharmacologically active compound family. *Spectrochimica Acta Part A: Molecular and Biomolecular Spectroscopy*, 74(5):1031–1045, 2009, doi:10.1016/j.saa.2009.07.015.

[29] R. Mohamed Asath, R. Premkumar, T. Mathavan, and A. Milton Franklin Benial. Structural, spectroscopic and molecular docking studies on 2-amino-3-chloro-5-trifluoromethyl pyridine: A potential bioactive agent. *Spectrochimica Acta Part A: Molecular and Biomolecular Spectroscopy*, 175:51–60, 2017, doi:10.1016/j.saa.2016.11.037.

[30] Salah MA Ridha, Zahraa Talib Ghaleb, and Abdulhadi Mirdan Ghaleb. The computational investigation of ir and uv-vis spectra of 2-isopropyl-5-methyl-1, 4-benzoquinone using dft and hf methods. *East European Journal of Physics*, (1):197–204, 2023, doi:10.26565/2312-4334-2023-1-18.

[31] Salah MA Ridha, Zahraa Talib Ghaleb, Abdulhakim Shaker Mohammed, and Abdulhadi Mirdan Ghaleb. Natural bond orbital (nbo) analysis of 1-(2-chloroethyl)-3-cyclohexyl-1-nitrosourea molecule based

on dft calculations. In *AIP Conference Proceedings*, volume 3282, page 050072. AIP Publishing LLC, 2025, doi:10.1063/5.0206825.

[32] Ibrahi Omotayo Asiata, Dyebamijis Abel Kolawole, and SEMIRE Banjo. Molecular charge distributions, vibrational frequency and stability studies on lh-indoie-3-carbaldehyde and (z)-indol-3-ylidenemethanol: Dft approach. *Iraqi National Journal Of Chemistry*, 18(1), 2018.

التوصيف الهيكلي والإلكتروني لقاعدتين من قواعد شيف مشتقتين من الإندول: دراسة تجريبية ومستندة إلى نظرية الدالية للكثافات (DFT)

* زهراء طالب غالب، نجلاء جليل خليل، نشوان عمر تاباشي

قسم الكيمياء، كلية العلوم، جامعة كركوك، كركوك، العراق

* الباحث المسؤول: *zahra@uokirkuk.edu*

الخلاصة

تتناول هذه الدراسة توليف وتوصيف مشتقات الإندول $(C_{17}H_{15}N_3O)$ و $(C_{17}H_{14}BrN_3O)$ باستخدام نظرية وظيفية الكثافة. وقد أُجريت عمليات التوصيف التجريبي للمركبات المُصنَعة الناتجة عن تكوين الهيدرازونات باستخدام تقنيات الأشعة تحت الحمراء والأشعة فوق البنفسجيةالمرئية، مما أدى إلى الحصول على معلومات حول المجموعات الوظيفية، والانتقالات الإلكترونية، والخصائص الهيكلية. استُخدمت حسابات $DFT/B3LYP$ باستخدام مجموعتي الأساس $(STO-3G^*)$ و $(3-21G)$ لتحسين الهندسة الجزيئية وتوزيع شحنة موليكن ومحاكاة الطيف الاهتزازي وطاقات المدارات. من مقارنة مجموعتي الأساس، تبين أن $(3-21G)$ يمكنها إنتاج نتائج أقرب إلى النتائج التجريبية خاصة بالنسبة لطول الرابطة وتردد الاهتزاز والانتقالات الإلكترونية. وبناءً على ذلك، فإن الاستخدام المشترك للطريقتين يوفر تحديد المعلمات الهيكلية بأقصى دقة، وتفسيرات توزيع الشحنة بأقصى موثوقية، وفهمًا أفضل لاستقرار الجزيء. ويؤكد هذا النهج المشترك بشكل أكبر على الدور الذي تلعبه الكيمياء الحسابية في استكمال وإثبات الملاحظات الطيفية للأنظمة المكونة من حلقات غير متجانسة مثل مشتقات الإندول. نلاحظ توافقاً جيداً بين النتائج النظرية والتجريبية فيما يتعلق بالخصائص الهيكلية والإلكترونية، حيث يبلغ طول الموجة القصوى (λ_{max}) لطيف الامتصاص في نطاق الأشعة فوق البنفسجية والمرئية (النظرية) 268.95$(DFT/B3LYPSTO-3G^*)$ نانومتر 282.92 $3-21G-3$ نانومتر، تجريبي - 282 نانومتر) للمركب الأول و((نظرية)($DFT/B3LYP$ ، 286.85 $STO-3G^*-3$ نانومتر، 289.24 $3-21G-3$ نانومتر، تجريبي - 288 نانومتر)) للمركب الثاني.

الكلمات الدالة: $(C_{17}H_{15}N_3O)$ (مشتق هيدرازون قائم على الإندول)، و $(C_{17}H_{14}BrN_3O)$ (هيدرازون إندول مُستبدل بالبروم)، الخصائص الهيكلية، $DFTUV-VisFT-IRTD-DF$.

التمويل: لا يوجد

بيان توفر البيانات: جميع البيانات التي تدعم نتائج الدراسة المقدمة متاحة من المؤلف المسؤول عند الطلب.

اقرارات:

تضارب المصالح: يقر المؤلف انه ليس لديهم تضارب في المصالح.

الموافقة الأخلاقية: طبيعة هذه الدراسة لا تتطلب الحصول على موافقة اخلاقية.

مساهمات المؤلفين: قامت زهراء طالب غالب بتصميم الدراسة والاشراف على العمل البحثي وكتابة المخطوطة. قام جميع الؤلفين بقراءة النسخة النهائية والموافقة عليها.